

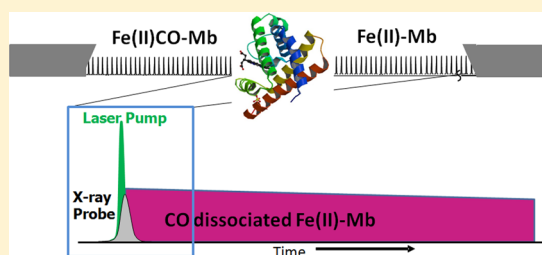
# Detailed Transient Heme Structures of Mb-CO in Solution after CO Dissociation: An X-ray Transient Absorption Spectroscopic Study

Andrew B. Stickrath,<sup>†</sup> Michael W. Mara,<sup>†,‡</sup> Jenny V. Lockard,<sup>†,§</sup> Michael R. Harpham,<sup>†</sup> Jier Huang,<sup>†</sup> Xiaoyi Zhang,<sup>†</sup> Klaus Attenkofer,<sup>†,||</sup> and Lin X. Chen<sup>\*,†,‡</sup>

<sup>†</sup>Chemical Sciences and Engineering Division and X-ray Sciences Division, Advanced Photon Source, Argonne National Laboratory, 9700 South Cass Avenue, Lemont, Illinois 60439, United States

<sup>‡</sup>Department of Chemistry, Northwestern University, 2145 Sheridan Road, Evanston, Illinois 60208, United States

**ABSTRACT:** Although understanding the structural dynamics associated with ligand photodissociation is necessary in order to correlate structure and function in biological systems, few techniques are capable of measuring the ultrafast dynamics of these systems in solution-phase at room temperature. We present here a detailed X-ray transient absorption (XTA) study of the photodissociation of CO-bound myoglobin (Fe(II)CO-Mb) in room-temperature aqueous buffer solution with a time resolution of 80 ps, along with a general procedure for handling biological samples under the harsh experimental conditions that transient X-ray experiments entail. The XTA spectra of (Fe(II)CO-Mb) exhibit significant XANES and XAFS alterations following 527 nm excitation, which remain unchanged for >47  $\mu$ s. These spectral changes indicate loss of the CO ligand, resulting in a five-coordinate, domed heme, and significant energetic reorganization of the 3d orbitals of the Fe center. With the current experimental setup, each X-ray pulse in the pulse train, separated by  $\sim$ 153 ns, can be separately discriminated, yielding snapshots of the myoglobin evolution over time. These methods can be easily applied to other biological systems, allowing for simultaneous structural and electronic measurements of any biological system with both ultrafast and slow time resolutions, effectively mapping out all of the samples' relevant physiological processes.



## INTRODUCTION

Myoglobin (Mb) has long been regarded as the hydrogen atom of proteins.<sup>1</sup> This metaphor is apt not only in regard to its relative simplicity in comparison with other proteins, its suitability for study with a variety of techniques, demonstrated most effectively for the studies presented here, and lability of diatomic adducts but also in regard to the richness of science to be discovered upon peeling back each layer. Although the basic function of storing and transporting diatomic oxygen and the general cycle of operation are well characterized,<sup>2–5</sup> there have been surprising recent discoveries related to biologically important functions beyond oxygen storage, including both an NO scavenging function and an NO evolving function in the heart of mammals.<sup>1,6–10</sup>

For each of these functions, the basic nature of diatomic molecular ligation and how it is mediated by the heme site/protein structural matrix and electronic environment is of fundamental importance in understanding enzymatic functions. These functions are essential not only for myoglobin but also for synthetic heterogeneous and homogeneous catalytic systems where the substrates are adsorbed or dissociated from catalytic sites. Although many studies have exquisitely inferred structural changes during the function of the protein, i.e., the ligation process, only recently has it become possible to probe such structural changes directly on the relevant time scale because of the availability of intense and short X-ray pulses

from third generation synchrotron sources. Pioneering work by Moffatt, Anfinsen, and their co-workers revealed motions of the heme site and its surrounding Mb protein matrix due to the CO photodissociation.<sup>11–14</sup> In particular, Anfinsen and co-workers studied the CO photodissociation from Mb in solution on a 75 ps to 10 ms time interval, monitoring both larger scale tertiary structural changes in the protein matrix and competition dynamics between geminate recombination and CO migration out of the heme pocket into the bulk solvent.<sup>14</sup>

Complementary to the X-ray transient diffraction studies, X-ray transient absorption (XTA) spectroscopy simultaneously monitors both the electronic changes in the iron heme center and the structural changes that occur locally about the iron center itself; both electronic and structural information are necessary to understand the structure/function relationship in myoglobin. In particular, the structural changes that occur in the heme following ligand loss, CO dissociation in this case, are associated with redistribution and spin-crossing among electrons of iron in 3d molecular orbitals (MOs). X-ray absorption near edge structure (XANES) spectra at the iron K-

**Special Issue:** Paul F. Barbara Memorial Issue

**Received:** August 31, 2012

**Revised:** November 15, 2012

**Published:** November 15, 2012



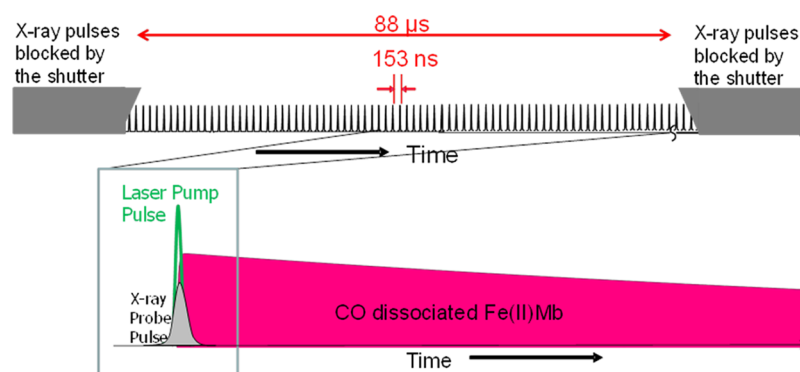


**Figure 1.** Timing structure of the XTA experiments at Beamline 11IDD, APS. Only a fraction of the 6.5 MHz repetition rate X-ray pulse train is allowed to illuminate the sample to protect against X-ray induced degradation. An optical chopper is used to limit the flux incident on the sample to approximately 10% of the total flux. The laser pump pulse is in the middle of the time window defined by the chopper temporal opening.

edge clearly reveal these electronic properties through shifts in transition edge energy, as well as energy shifts and intensity variation of pre-edge peaks, revealing detailed electronic configuration information not readily available from most optical methods. Furthermore, the X-ray absorption fine structure (XAFS) spectrum is extremely sensitive to minute local geometric alterations around the Fe center, resulting in atom–atom distance measurements with 0.01–0.02 Å resolution. Although previous pump–probe experiments have shown the significant photoinduced changes that occur around the Fe K-edge, in particular the pioneering works of Mills<sup>15</sup> and recent work of Lima et al.,<sup>16</sup> a full analysis of the structural dynamics via the XAFS portion of the spectrum has not yet been performed.

The experiments presented here, following the evolution of the immediate heme environment upon photodissociation of CO, entail both aspects of the Mb paradigm: using the molecule as a test mule to establish an extension of the XTA spectroscopic technique to biological systems, starting from the protein domain, the first such example at the APS, and performing fundamental studies of the heme electronic and structural rearrangement on both ultrafast and slow time scales. With the establishment of X-ray free electron lasers, capable of generating high-flux X-rays with subpicosecond pulse widths, these new experimental procedures pave the way for structural measurements as the ligand photodissociates. Such knowledge remains a key component in the understanding of the structure/function correlation not only in Mb but in biological systems as a whole.

## ■ EXPERIMENTAL METHOD

**1. Sample Preparation and Handling.** Horse skeletal metmyoglobin, Fe(III)Mb, was purchased from Sigma-Aldrich in a lyophilized form and was used without further purification. Mb was prepared at 4 mM concentration in a 0.1 M potassium phosphate buffer solution (pH ~7.1) in 20 mL aliquots, each of which serves as one solution batch for the sample circulating system in the experiment. Reduced Fe(II)Mb, with the CO ligand bound, was prepared by the following procedure: (1) a 19.5-mL Mb solution was first purged with dry nitrogen gas to remove oxygen in the presence of a few drops of polypropylene glycol as the defoaming reagent for 15 min; (2) 0.5 mL of 0.5 M sodium dithionite ( $\text{Na}_2\text{S}_2\text{O}_4$ ) was then added to the Mb solution (molar ratio of  $\text{Na}_2\text{S}_2\text{O}_4$  to Mb of 6.4:1) to reduce Fe(III) to Fe(II) at the heme site; and (3) the ligation of Fe(II) with CO was accomplished by passing CO gas through the

solution for at least 20 min in a sealed sample environment (only the gas outlet vented through the ventilation system) before the XTA measurements. Following the initial sample purge, a slight positive pressure of carbon monoxide was maintained at all times through the end of the experiment to ensure an inert atmosphere. The formation of ~100% Fe(II)CO-Mb was confirmed by a UV–vis spectrum and the static XAFS spectrum of the sample solution, which agreed with the literature.<sup>17</sup> The heme iron oxidation state and protein degradation were monitored during data collection by careful comparison of the XANES spectrum with the known, steady-state Fe(II)CO-Mb spectrum,<sup>18</sup> to ensure sample stability under experimental conditions.

**2. X-ray Transient Absorption (XTA) Setup.** XTA spectra were collected at the inline dual undulator beamline 11-ID-D of the Advanced Photon Source (APS).<sup>19–23</sup> A sample chamber hosting a liquid jet, sealed sample circulation system, and X-ray fluorescence detectors was used as in our previous XTA experiments.<sup>20,24,25</sup> Modifications were made to accommodate protein solution samples and CO atmospheric environment in a sealed sample chamber. One important improvement was to extend the length of the HPLC tubing used as the jet nozzle to as long as 10 cm to establish a fast laminar flow (a nozzle with a diameter of 0.7 mm, a flow rate of ~50 mL/min) which allows fresh sample volumes to be excited by consecutive laser pulses at 1 kHz repetition rate. Under such conditions, only the pumped volume was probed through the 47-μs delay time window (see below) for data collection following each laser excitation pulse. The liquid jet diameter was ~0.7 μm at the pump/probe interaction region, resulting in a pump absorbance of OD ~3 at 527 nm. The rest of the sample recirculating system consists of a closed loop of Teflon tubing driven by a peristaltic pump. The sample solution was maintained at ~5 °C with a custom built reservoir cooled by chilled water. As described earlier, X-ray fluorescence signals were collected by custom built APD detectors. A Z-1 filter/soller slit combo was attached in front of each detector element with six absorption lengths of MnO filter to remove most of the elastic scattering signal. A 25-μm thick black polyimide film was placed in front of the Z-1 filter to protect it and block scattered laser light from reaching the APD detectors.

Since the CO photodissociation and subsequent CO recombination with Fe(II)Mb are known to exhibit rich structural dynamics on time scales ranging from femtosecond to subsecond, it was desirable to collect transient data both on the fastest time scale possible at a synchrotron source as well as

within the longest time window possible. The 24-bunch mode operation of the APS used in these experiments produces X-ray pulse of  $\sim 80$  ps (fwhm) at  $\sim 6.5$  MHz repetition rate. The APD outputs were connected to two fast analyzer cards (Agilent), where signals from 307 pulses in the entire X-ray pulse train were individually digitized. The pulse shape, signal offset, and dark counts were recorded, and used for an in situ curve fitting procedure (G. Jennings). In initial experiments, we found that the protein starts to degrade within 20–40 min when the full X-ray pulse train (average flux of  $\sim 10^{13}$  photons/s) was used. Because data acquisition with this concentration of Mb generally requires several hours, this sample degradation makes room temperature, solution-phase XTA measurements rather difficult. In order to circumvent this challenge, we inserted in the X-ray beam path before the sample jet an optical chopper synchronized with the incident X-ray pulses. The chopper was modified for X-ray use by stacking multiple blades at different relative orientations for an adjustable opening. The chopper blade setting was chosen to allow  $\sim 10\%$  of the X-ray pulse train to reach the sample. After accounting for synchronization jitter between the X-ray pulses and the open time of the chopper, a temporally clear aperture of  $\sim 88 \mu\text{s}$  was achieved (Figure 1). The laser pump pulse was timed to arrive  $\sim 40 \mu\text{s}$  into this time window, resulting in  $\sim 47 \mu\text{s}$  of temporal probing following photodissociation, with the first probe pulse arriving  $\sim 100$  ps after the pump and each subsequent pulse arriving at the APS 6.5 MHz repetition rate, i.e., with a pulse-to-pulse time interval of 153 ns. The  $\sim 40 \mu\text{s}$  “ground-state window” prior to excitation allows 264 bunches to be averaged to produce the ground-state Fe(II)CO-Mb spectrum, whereas each subsequent pulse is associated with a particular time delay. The reduced total X-ray flux by the chopper application greatly prolonged the sample durability and enabled the collection of a sufficient number of scans to achieve reasonable data quality. Each energy point was then averaged for 4 s, and a total of 97 scans were averaged to generate the final data set. Although the top-up operation of the APS ensures a constant average flux, the flux of individual pulses may vary significantly from each other. Therefore each pulse was individually normalized with a third APD detector placed upstream of the sample jet, collecting elastic scattering X-ray signals from a piece of 25- $\mu\text{m}$  thick polyimide film. The output of each APD detector was integrated for four seconds per energy point, amplified to  $\sim 10$  mV magnitude and digitized by the fast analyzer card (Agilent).

The photodissociation of CO was induced by a laser pulse ( $\sim 0.7$  mJ/mm<sup>2</sup>) at 527 nm. The laser system has been described previously.<sup>19,21</sup> Briefly, an oscillator (Time-Bandwidth) produced a train of seed pulses at 1.053  $\mu\text{m}$ , 5 ps duration (fwhm) and synchronized to an  $\sim 88$  MHz sinusoidal signal derived from one-quarter of the synchrotron RF frequency,  $\sim 356$  MHz. The seed pulses were directly injected into a custom-built Quantronix Nd:YLF regenerative amplifier, and were amplified to about 2 mJ/pulse at 1 kHz repetition rate. The laser beam from the amplifier at 1.053  $\mu\text{m}$  was then frequency-doubled to 527 nm and focused to a  $\sim 1$ -mm diameter spot at the sample jet. The X-ray beam was focused to a rectangular shape of 0.5 mm (H)  $\times$  0.2 mm (V) by a set of focusing mirrors. Timing and relative delay between the laser and X-ray pulses were controlled with an electronic delay generator (Colby Instruments).

## RESULTS AND DISCUSSIONS

**1. Transient Electronic Configurations and Energy Levels of Heme Iron in Mb-CO.** The heme Fe K-edge XANES spectra in horse skeletal myoglobin are shown in Figure 2 for the starting Fe(III)Met-Mb, CO saturated

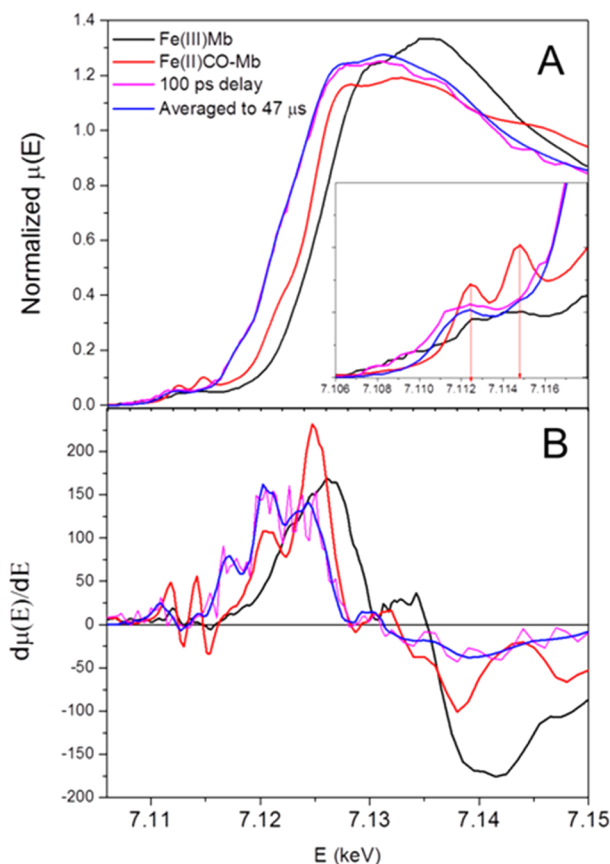


**Figure 2.** (A) XANES spectra of heme iron at Fe K-edge for different states of horse muscle myoglobin; (B) the first derivatives of XANES spectra in panel A.

Fe(II)CO-Mb, and photodissociated deoxy-Fe(II)-Mb, with the pre-edge region highlighted in the inset. The transition edge positions defined by the first inflection point at the edge for deoxy-Fe(II)-Mb, Fe(II)CO-Mb, and Fe(III)Met-Mb are 7.1170, 7.1207, and 7.1256 keV, respectively, demonstrating clear distinctions among them and a progressive edge shift to higher energies due to the iron electron density change. Hence the dynamics of the state-to-state change can be monitored at the transition edge. The edge position for photolyzed Fe(II)CO-Mb obtained from the X-ray pulse immediately after the laser pulse, the “sync pulse”, although noisier due to only a single bunch contributing to the single averaging, has almost perfect overlap with those averaged over 153 ns to 47  $\mu\text{s}$ , suggesting that the heme iron electronic structure is consistent from 100 ps to tens of microseconds after the laser pulse that triggered dissociation. Such an assessment is also confirmed by examining the pre-edge region of the XANES spectra as described below.

The pre-edge spectral features of Fe have been comprehensively documented by Solomon and co-workers over tens of ferric and ferrous model compounds with various numbers of ligands and coordination geometry.<sup>26</sup> Their studies showed characteristic pre-edge features and their relative intensities



originated from quadrupole-allowed  $1s \rightarrow 3d$  molecular orbital transitions associated with different coordination geometries and oxidation states of iron. Based on these studies, the iron pre-edge features in different states of Mb (Figure 2A, inset) can be rationalized by quadrupole-allowed transitions from  $1s$  to one of the vacated  $3d$  molecular orbitals shown in Figure 3, especially for the iron site electronic structural changes within 100 ps of the photolysis triggering laser pulse.

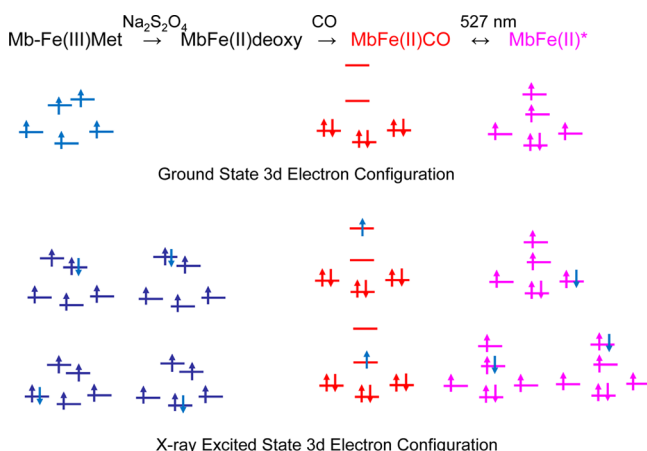


**Figure 3.** Sample processing steps and the 3d electronic configurations corresponding to different states of Mb involved in the study.

As previously observed and expected<sup>17,18,27</sup> for the iron in the starting Fe(III)-Met-Mb ( $3d^5$ ) state, six weak field ligands are ligated by iron: four N atoms from the porphyrin macrocycle, one O from a water molecule, and one N from the imidazole of His93, giving two experimentally observed weak pre-edge peaks at 7.1126 and 7.1148 keV. Such features fit what have been observed for an octahedral ferric center in a nearly total symmetric octahedral geometry with a ground state electronic configuration of  $(3d_{xy})^1 (3d_{yz})^1 (3d_{xz})^1 (3d_z)^1 (3d_{x^2-y^2})^1$ . The two weak pre-edge features are due to five possible transitions of  $1s \rightarrow (3d_{xy})^1, (3d_{yz})^1, (3d_{xz})^1, (3d_z)^1$ , or  $(3d_{x^2-y^2})^1$  (Figure 3) with an approximate energy difference between the pseudo  $t_{2g}$  and  $e_g$  MOs of 2.2 eV; the energy differences between  $(3d_z)^1$  and  $(3d_{x^2-y^2})^1$  or among  $(3d_{xy})^1, (3d_{yz})^1, (3d_{xz})^1$  cannot be resolved due to the energy resolution limit of the X-ray monochromator. The results agree with those obtained for Fe(III) compounds with octahedral geometry and asymmetric ligands along the  $z$  direction; in this case, due to the difference between the  $\text{H}_2\text{O}$  and imidazole ligands above and below the heme macrocycle.

Two sharp pre-edge features are present in the Fe(II)CO-Mb spectrum (Figure 2A inset). Because of the ligation of iron with a strong field ligand, CO, the energy splitting between  $(3d_{xy})^1 (3d_{yz})^1 (3d_{xz})^1$  and  $(3d_z)^1 (3d_{x^2-y^2})^1$  is increased significantly, resulting in a low spin state ferrous center with an electronic configuration of  $(3d_{xy})^2 (3d_{yz})^2 (3d_{xz})^2 (3d_z)^0 (3d_{x^2-y^2})^0$ . Meanwhile, due to the bonding difference between CO and imidazole ligands, the electron density along the  $z$  axis is asymmetric, matching the  $p$  MO symmetry. Hence the vacant  $3d_z$  MO can mix with the  $4p$  MO resulting in slightly dipole-allowed  $1s \rightarrow 3d$  transitions, manifesting in enhanced pre-edge intensities which appear as two sharp features at 7.1125 and 7.1148 keV (Figure 2A inset). These two features are attributed to  $1s \rightarrow 3d_z^2$  and  $1s \rightarrow 3d_{x^2-y^2}$  transitions, and hence provide an

estimated energy splitting of  $\sim 2.3$  eV between the two high energy  $3d$  MOs when heme is ligated with CO.

Limited by the 80-ps X-ray pulse duration of the synchrotron source, the spectra of photodissociated deoxy-Fe(II)-Mb\* were obtained by collecting fluorescence signals resulting from each X-ray pulse transmitted through the chopper, with the laser pulse synchronized to arrive  $\sim 100$  ps before a select X-ray pulse, defined as the “sync pulse”. The signals from subsequent X-ray pulses separated by 153 ns time intervals were also collected up to  $\sim 47 \mu\text{s}$  after the laser pulse, giving approximately 300 useable pulses in the pulse train. The most significant change in the XANES spectra of deoxy-Fe(II)-Mb taken from signals of different X-ray pulses after the “sync pulse” is the disappearance of the two sharp pre-edge features mentioned above, which are replaced by a much weaker, broader and red-shifted pre-edge feature compared to those of Fe(II)CO-Mb. The XANES spectra from longer delay times, obtained from the subsequent X-ray pulses, are nearly identical to that of the “sync pulse”, as seen in the time evolution of the difference signals at two characteristic energies of 7.123 and 7.146 keV, respectively (Figure 4).

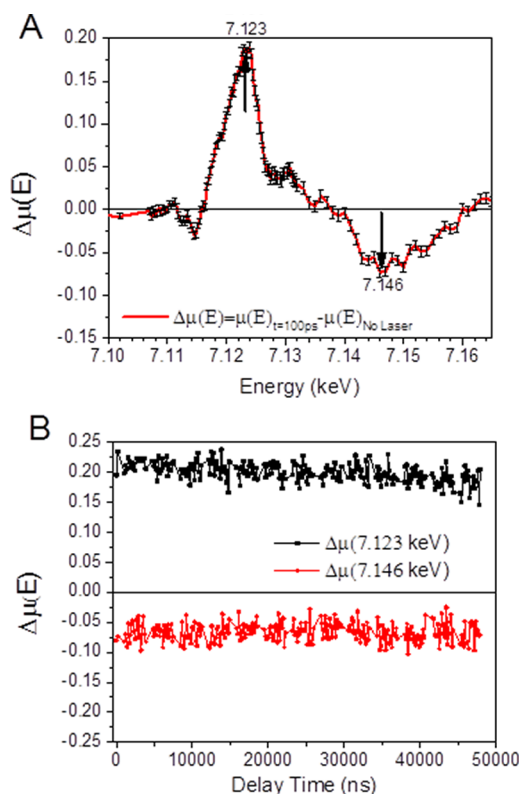


**Figure 4.** (A) Difference XANES between the ground state Fe(II)CO-Mb and photodissociated Mb within 100 ps from the laser pump pulse; (B) the respective intensity signal differences at 7.123 and 7.146 keV, where the largest difference signals are present, as a function of the delay time showing no obvious structural evolution after the first 100 ps following photoexcitation.

The minimal variation of the XANES spectra over the  $47 \mu\text{s}$  measurement window implies that most of the structural changes in the iron site of heme are finished already within the first 100-ps after the photoexcitation and are maintained for  $>47 \mu\text{s}$ . For this reason, the resulting photodissociated Fe(II)-Mb spectrum is constructed from signals summed/averaged over 300 pulses at delays from 153 ns to  $47 \mu\text{s}$  (Figure 2 in

blue) and is used to obtain the transient structural details after the photodissociation. The observed spectral changes can be rationalized by considering CO dissociation from the heme iron site transforming the iron from a low-spin ferrous, pseudo-octahedral coordination geometry to a high-spin ferrous, square pyramidal coordination geometry. The energy splitting between pseudo  $t_{2g}$  and  $e_g$  MOs decreases significantly after the strong-field ligand CO leaves. The possible  $1s \rightarrow 3d$  transitions in the photodissociated electronic configuration are shown in Figure 3 and agree with the shape of the pre-edge features observed in the experiment. Compared with the pre-edge features at 100 ps delay, the pre-edge features from the averaged spectrum are only slightly narrower. This subtle difference suggests a dynamic structural distortion of the heme macrocycle which could result from vibrational relaxation or heating and produces local structural and energetic fluctuations in 3d MOs as observed in our previous studies of nickeltetramesitylporphyrin (NiTMP).<sup>21,28,29</sup> From 100-ps delay and then on, the heme structure has finished transformation to a domed, square pyramidal coordination geometry as shown in the X-ray diffraction studies of wild type Mb by Anfinsen and co-workers.<sup>30</sup> Thus, the pre-edge features reflect the equilibrated domed heme with a slightly narrower bandwidth. The structural changes after the first 100 ps of CO dissociation, if any, are too small to be characterized in the time window up to 47  $\mu$ s.

The above results agree with what has been described in previous reports. According to the literature,<sup>31–33</sup> CO photodissociation and heme relaxation take place on the ultrafast time scale. The Fe–C bond breaks  $\leq 50$  fs, accompanied by displacement of the Fe center by  $\sim 0.3$  Å, as demonstrated by ultrafast transient absorption,<sup>31</sup> resonance Raman,<sup>32</sup> and two-color photon echo measurements.<sup>33</sup> On this time scale the heme center also undergoes a metal-to-ring charge transfer, moving electron density from the iron center to the  $\pi$  orbitals of the porphyrin. After  $\sim 300$  fs, ring-to-iron back charge transfer results in an iron center with a nonequilibrium d-orbital population and a porphyrin with an essentially ground-state electronic configuration.<sup>31,33</sup> The iron center will relax to the ground state after  $\sim 3$  ps. There is also further motion in the proximal His93 which is effectively transmitted to the protein and lasts for up to 100 ps<sup>32</sup> and is likely associated with large-scale protein motions necessary to open transient pathways for the release of the CO which are beyond the spatial scale for the XTA method described here. Hence the most drastic structural dynamics around the iron center are completed well before 100 ps delay, and require pulsed X-rays with much shorter durations than those typically available from most third-generation synchrotrons for transient structure determination.

Before the current study, we had hoped to see structural changes around the heme iron site evolving in time on a sufficiently long time scale after the initial CO dissociation such as to be observable with the given experiment restrictions:  $\sim 80$ -ps resolution defined by the X-ray pulses; and  $\sim 47$   $\mu$ s temporal window defined by the optical chopper. Previous studies indicated that, although the CO was dissociated from the heme very quickly upon excitation, the CO remained in the distal pocket for much longer.<sup>11,14</sup> Ejection of the CO from the protein core competed with geminate recombination, which had time constants of  $(220 \text{ ns})^{-1}$  and  $(5.8 \text{ } \mu\text{s})^{-1}$ , respectively for sperm whale Mb.<sup>14</sup> Moreover, it has been also documented that the CO release time constant was 700 ns for horse heart Mb.<sup>34</sup> However, CO typically exhibits little geminate recombination, unlike  $\text{O}_2$  or NO, due to its high barrier to

recombination. CO will return nongeminately into the core of the protein with a bimolecular rate constant of  $1.9 \times 10^7 \text{ M}^{-1} \text{ s}^{-1}$  and will eventually return to the heme on the millisecond time scale.<sup>14</sup> Therefore, it is not surprising that the iron heme site retains the same structure up to 47  $\mu$ s after the CO dissociation.

**2. Geometric Changes of Heme in Mb During/After the CO Photodissociation.** The geometric changes of heme iron during/after the photodissociation of CO have been extracted through XAFS data analyses of transient spectra taken with a time resolution limited by the X-ray pulses from the APS, i.e., 80–100 ps. Because of the striking resemblance of the XAS spectrum within 100 ps delay with those of spectra taken at later time up to 47  $\mu$ s after the laser pump pulse, we reason that the heme iron structure at 100 ps delay is already similar to the final structure of Fe(II)-Mb, and we can average the spectra of photodissociated Fe(II)-Mb obtained from the  $\sim 300$  X-ray pulses in the pulse train that trail the laser pump pulse. Hence, the averaged signal intensity at each energy point is from a total number  $1.19 \times 10^8$  X-ray pulses (note:  $1.19 \times 10^8 = 4000$  (4 s/point at 1 kHz rep. rate)  $\times 97$  (scans)  $\times 307$  (pulses after the photoexcitation)), which is equivalent to 18 s/point, if the full X-ray flux at the sample (i.e.,  $\sim 10^{13}$  photons/s at 7 keV) is used. There are 306 energy points in each scan, so the full scan with the same signal-to-noise level will take 5,500 s, or  $>1.5$  h. In comparison, each data point in the spectrum obtained from the “sync pulse” is the result of 0.058 s integration time if the full beam is used. An XAFS spectrum with high signal-to-noise ratio for the intermediate structure after the CO photodissociation is shown in Figure 5 where the spectral differences

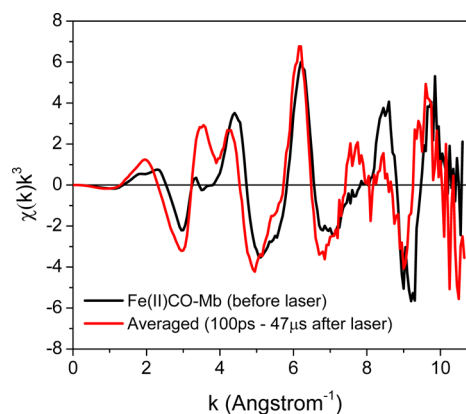


**Figure 5.** XAFS spectra of Fe(II)COMb before and after the photoexcitation. The spectrum after the photoexcitation is an average of signals from 307 pulses after the excitation as described in the text.

before and after the photodissociation are evident. Because the averaged photodissociated Fe(II)-Mb spectrum has a rather high signal-to-noise ratio, the FT windows of  $k = 2.5 - 10.5$  Å<sup>−1</sup> were chosen for both spectra of Fe(II)CO-Mb before the laser pulse and Fe(II)-Mb averaged over 307 pulses after the laser and with the 30% ground state contribution removed. The XAFS spectra in Figure 5 were subsequently Fourier-transformed into FT-XAFS spectra in Figure 6 and fit in R-space. The remaining ground state Fe(II)CO-Mb after the laser pulse excitation was determined to be  $\sim 30\%$  of the total population according to the pre-edge feature differences between Fe(II)-CO-Mb and Fe(II)-Mb. This ground-state contribution has been removed from the Fe(II)-Mb spectra in Figures 5 and 6.

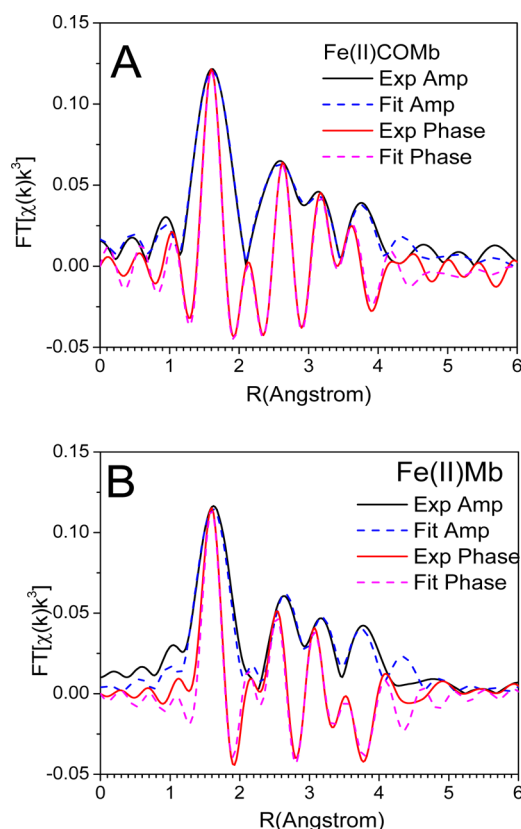


**Figure 6.** FT-XAFS spectra and fits for (A) Fe(II)CO-Mb and (B) after photoexcitation.

Using WinXAS as a fitting program,<sup>35</sup> the FT-XAFS spectra of Fe(II)CO-Mb and Fe(II)-Mb were fit to the corresponding calculated spectra using FEFF8.2<sup>36</sup> according to the crystal structure of the same protein from the Protein Data Bank (PDB structure code: 3jr6)

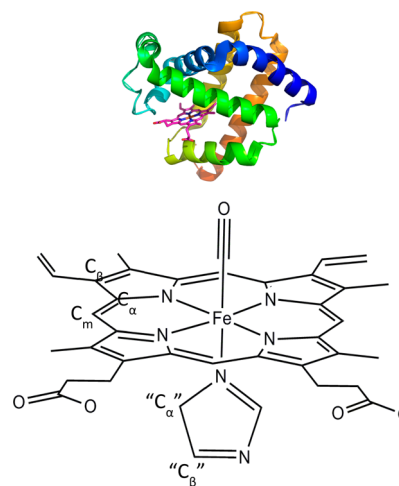
The fits were conducted based on scattering pathways computed by the FEFF8.2 program.<sup>37</sup> The postedge oscillations in the XAFS spectrum are caused by interference patterns due to the outgoing and back scattered photoelectron waves originating from the X-ray absorbing atom and nearby scattering atoms. The Fourier transform of this interference pattern gives a radial distribution function centered about the Fe atoms, where the peaks represent different atom–atom distances. By fitting a theoretical model to the experimental data, the structural parameters corresponding to the structure of the molecule can be extracted.<sup>38–40</sup> The XAFS portion of the spectrum is modeled using the equation<sup>38</sup>

$$\chi(k) = \sum_i \frac{F_{\text{eff}}(k) S_0^2(k) N_i}{k R_i^2} \exp^{-2k^2 \sigma_i^2} \sin[2k R_i + \phi_i(k)]$$

where  $F_{\text{eff}}(k)$  is the backscattering amplitude,  $N_i$  is the coordination number,  $R_i$  is the atom–atom distance, and  $\sigma_i$  is the Debye–Waller factor. Using this equation, it is clear that the oscillations obtained from the XAFS spectrum can be fit to a sum of scattering paths from each atom in the theoretical model.

The coordination numbers for Fe(II) with neighboring atoms were fixed according to the known structures (Scheme 1). Limited by the number of data points and the signal-to-noise ratio of the spectra, too many fitting parameters with similar values could cause overdetermination of the structural

**Scheme 1.** Top: Horse Heart Muscle Myoglobin Structure from the Protein Data Bank (3jr6); Bottom: Iron Protoporphyrin IX, with All Relevant Scattering Paths Labeled<sup>a</sup>



<sup>a</sup>Note that, for  $C_\alpha$  and  $C_\beta$ , 8 carbons for each are located in the porphyrin ring, and two more in the imidazole of the histidine. The  $N_3$  of the histidine is treated as a C center, since C and N are essentially indistinguishable in XAFS fitting.

parameters. Due to the similarity in the five member imidazole ring of His93 and the five-member pyrrole rings in the porphyrin, symmetry related multiple scattering pathways with similar distances were grouped as five equivalent paths used in the fitting. The approximation is justified by insignificant improvement of the residuals compared to the fits with additional paths. All single scattering pathways with the Fe-atom distance up to 4.5 Å are listed in Table 1, and an image of iron protoporphyrin IX with all relevant scattering paths is found in Scheme 1. Because the Fe–N distances in the porphyrin core and to the imidazole ring of His93 are similar, a coordination number (CN) of 5 is used in the fitting. Similarly, paths of Fe– $C_\alpha$  and Fe– $C_\beta$  and equivalent in the imidazole ring are also considered to be degenerate with CN of 10. The CN for Fe– $C_\gamma$  remains 4. Multiple scattering paths through the CO ligand and the porphyrin macrocycle are also included in the fitting based on their weights calculated from the FEFF calculations. The forward focusing effect of Fe–C–O is significant based on the calculations and hence multiple scattering paths with three and four scatterers, such as Fe → C → O → Fe and Fe → C → O → C → Fe, have been counted for in the analysis. The other multiple scattering paths with the weights over 20% from the FEFF calculations were proven to be important in the fitting. The goodness of fits was judged by not only the amplitude but also the imaginary part of the function for the XAFS spectra as seen in Figure 6. Local structural parameters around the Fe(II) center for the ground state Fe(II)CO-Mb and its photo-dissociated product Fe(II)Mb in terms of Fe-to-atom distances have been extracted and listed in Table 1.

Comparing the heme structure of the ground state Fe(II)CO-Mb with the crystal structure, all of the Fe-to-atom distances obtained from XAFS measurements are 0.03 to 0.12 Å shorter, which is considered a reasonable agreement because of the 1.25 Å accuracy limit of the protein crystal structure from the Protein Data Bank (PDB, 3jr6). A good agreement between single crystal diffraction data and XAFS data is rare for the



Table 1. Iron Heme Structural Parameters<sup>a</sup>

	Fe(II)CO-Mb				Fe(II)-Mb			
	CN	R (Å) <sup>b</sup>	$\sigma^2$ (Å <sup>2</sup> ) <sup>c</sup>	$\Delta E$ (eV) <sup>d</sup>	CN	R (Å) <sup>b</sup>	$\sigma^2$ (Å <sup>2</sup> ) <sup>c</sup>	$\Delta E$ (eV) <sup>d</sup>
Fe–C(O)	1	1.76	0.0001	18.10				16.47
Fe–N(His,Heme)	5	1.99	0.0013		5	2.05	0.0042	
Fe–O(CO)	1	2.84	0.0002					
Fe–C <sub>α</sub>	10	3.08	0.0080		10	3.05	0.0034	
Fe–C <sub>m</sub>	4	3.38	0.0001		4	3.47	0.0010	
Fe–C <sub>β</sub>	10	4.41	0.0001		10	4.21	0.0023	

<sup>a</sup>The scattering scaling parameter  $S^2 = 0.9$ , and the residuals of the fits for Fe(II)CO-Mb is 8.11. <sup>b</sup>The experimental errors is  $\pm 0.02$  Å. <sup>c</sup>The errors are estimated to be  $<0.002$  Å<sup>2</sup> using the crystal structure as the reference in the FeFF calculations. <sup>d</sup>The  $E_0$  is relative to the metal foil in the FeFF calculations and the value represents the best overlap in the XAFS features between the calculated and experimental spectra.

metal site and has been shown to be only achievable with crystal structural resolution better than 0.9 Å.<sup>41,42</sup> The average Fe–N nearest ligand distance for deoxy-Fe(II)-Mb is 0.06 Å longer than Fe(II)CO-Mb, which suggests a domed square-pyramidal coordination which has the iron shifted above the plane formed by nitrogen atoms by about 0.5 Å, similar to those in the literature. The average iron-to-C<sub>α</sub> (the C atom directly connected to the N atom of the pyrrol rings) distance is essentially unchanged, whereas the average distances for the iron to C in the meta position (this C atom links two adjacent pyrrol rings), and to the C<sub>β</sub> atoms (the two distant C atoms in the pyrrol rings from the iron center) are respectively increased by 0.1 Å and decreased by 0.2 Å, indicating distortion of the whole macrocycle after photodissociation with respect to the structure before the laser pulse.

We then attempted to look more closely at the differences of XAFS spectra between the one averaged over 300 pulses following the photodissociation with those accumulated from single pulse signals at 100 ps and 153 ns delays after the laser pulse. As shown in Figure 7, the three-point smoothed single pulse spectrum and the averaged spectrum have only subtle differences. Due to the data quality limit for the single pulse signals, the Fourier-transformed XAFS spectra were taken from a relatively small  $k$  window of 1.7–6.7 Å<sup>−1</sup>, shown in Figure 7B. Although the subtle differences could not warrant a high precision data analysis even with the difference spectra, one can clearly identify the small shifts at the peak positions at different time delays in the spectra from the FT-XAFS. Admittedly, although the peak shift direction generally does not yield correct atomic distances without a full data analysis, it does show the trend of changes. Based on these results obtained so far, it is necessary to use the pump–probe approach with much shorter X-ray pulses to probe atomic movements and electron density shifts around iron site of heme during the CO photodissociation; such an approach is hence planned in the future studies.

## SUMMARY

We have succeeded in using the XTA spectroscopy to study a protein sample at relatively low concentration by employing a newly developed procedure based on an X-ray shutter combined with a sophisticated data acquisition scheme which allows signals from all X-ray pulses in the most common APS timing mode to be digitized, covering both ultrafast and slow time scales for many biological systems. Our results revealed that most of the immediate structural changes as the CO dissociates from the iron site are completed within 100 ps on an XAFS detectable spatial scale, and almost no structural change takes place during the  $\sim 47$  μs window following the CO

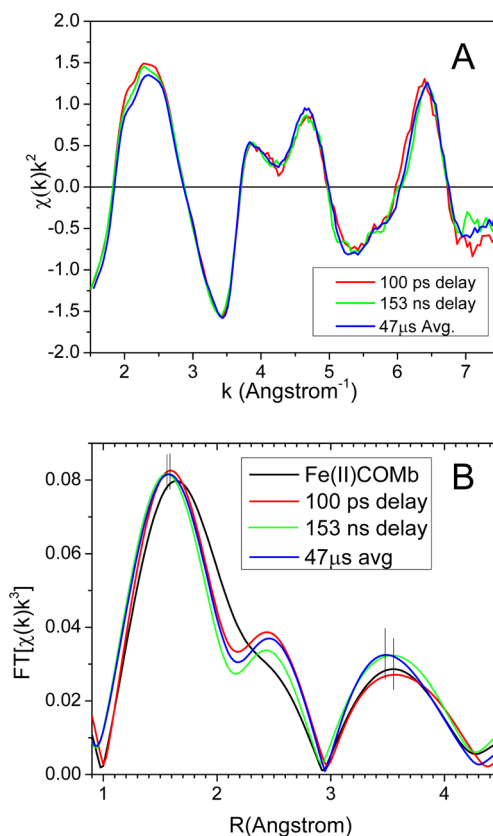


**Figure 7.** (A) XAFS spectra at 100 ps, 153 ns delays, and over 47 μs averaging and (B) FT-XAFS spectra taken from  $k = 1.7$ – $6.7$  Å<sup>−1</sup>.

dissociation. The detailed structural analysis revealed evidence of a domed heme structure where the iron stays out of the porphyrin plane by about 0.5 Å, as well as other distortions in the macrocycle. No evidence of CO recombination in the time window of the experiments was observed, although the recombination could exceed the time window of the experiments and become virtually asynchronous. This work opens opportunities for studying protein samples with the XTA method. The combined transient electronic/structural information extracted from XTA promises to impact not only myoglobin but biological systems and science as a whole.

## AUTHOR INFORMATION

### Corresponding Author

\*E-mail: lchen@anl.gov; l-chen@northwestern.edu. Phone: 630-252-3533; 847-491-3479.

## Present Addresses

<sup>§</sup>Department of Chemistry, Rutgers University—Newark, Newark, New Jersey 07102-1811.

<sup>||</sup>Photon Sciences Directorate, Brookhaven National Laboratory, Upton, New York 11973-5000.

## Notes

The authors declare no competing financial interest.

## ■ ACKNOWLEDGMENTS

Work at ANL was partially supported by the U.S. Department of Energy, Office of Basic Energy Sciences, Division of Chemical Sciences, Geosciences, and Biosciences, under Contract DE-AC02-06CH11357. Use of the Advanced Photon Source was supported by the U.S. Department of Energy, Office of Science, Office of Basic Energy Sciences, under Contract No. DE-AC02-06CH11357.

## ■ REFERENCES

- (1) Frauenfelder, H.; McMahon, B. H.; Fenimore, P. W. *Proc. Natl. Acad. Sci.* **2003**, *100*, 8615–8617.
- (2) Wittenberg, B. A.; Wittenberg, J. B. *Annu. Rev. Physiol.* **1989**, *51*, 857–878.
- (3) Parkhurst, L. J. *Annu. Rev. Phys. Chem.* **1979**, *30*, 503–546.
- (4) Olson, J. S.; Soman, J.; Phillips, G. N., Jr. *IUBMB Life* **2007**, *59*, 552–562.
- (5) Teeter, M. M. *Protein Sci.* **2004**, *13*, 313–318.
- (6) Flogel, U.; Merx, M. W.; Godecke, A.; Decking, U. K.; Schrader, J. *Proc. Natl. Acad. Sci. U.S.A.* **2001**, *98*, 735–740.
- (7) Merx, M. W.; Godecke, A.; Flogel, U.; Schrader, J. *FASEB J.* **2005**, *19*, 1015–1017.
- (8) Kreutzer, U.; Jue, T. *Pflugers Arch* **2006**, *452*, 36–42.
- (9) Hendgen-Cotta, U. B.; et al. *Proc. Natl. Acad. Sci.* **2008**, *105*, 10256–10261.
- (10) Totzeck, M.; et al. *Circulation* **2012**, *126*, 325–334.
- (11) Srajer, V.; Ren, Z.; Teng, T. Y.; Schmidt, M.; Ursby, T.; Bourgeois, D.; Pradervand, C.; Schildkamp, W.; Wulff, M.; Moffat, K. *Biochemistry* **2001**, *40*, 13802–13815.
- (12) Srajer, V.; Teng, T.; Ursby, T.; Pradervand, C.; Ren, Z.; Adachi, S.; Schildkamp, W.; Bourgeois, D.; Wulff, M.; Moffat, K. *Science* **1996**, *274*, 1726–1729.
- (13) Bourgeois, D.; Vallone, B.; Arcovito, A.; Sciara, G.; Schotte, F.; Anfinrud, P. A.; Brunori, M. *Proc. Natl. Acad. Sci. U.S.A.* **2006**, *103*, 4924–4929.
- (14) Cho, H. S.; Dashdorj, N.; Schotte, F.; Graber, T.; Henning, R.; Anfinrud, P. *Proc. Natl. Acad. Sci. U.S.A.* **2010**, *107*, 7281–7286.
- (15) Mills, D. M.; Lewis, A.; Harootunian, A.; Huang, J.; Smith, B. *Science* **1984**, *223*, 811–813.
- (16) Lima, F. A.; et al. *Rev. Sci. Instrum.* **2011**, *82*, 063111.
- (17) D'Angelo, P.; Lapi, A.; Migliorati, V.; Arcovito, A.; Benfatto, M.; Roscioni, O. M.; Meyer-Klaucke, W.; Della-Longa, S. *Inorg. Chem.* **2008**, *47*, 9905–9918.
- (18) Benfatto, M.; Della Longa, S.; Natoli, C. R. *J. Synchrotron Radiat.* **2003**, *10*, 51–57.
- (19) Chen, L. X.; Jennings, G.; Liu, T.; Gosztola, D. J.; Hessler, J. P. *J. Am. Chem. Soc.* **2002**, *124*, 10861–10867.
- (20) Chen, L. X.; Shaw, G. B.; Novozhilova, I.; Liu, T.; Jennings, G.; Attenkofer, K.; Meyer, G. J.; Coppens, P. *J. Am. Chem. Soc.* **2003**, *125*, 7022–7034.
- (21) Chen, L. X.; Jäger, W. J. H.; Jennings, G.; Gosztola, D. J.; Munkholm, A.; Hessler, J. P. *Science* **2001**, *292*, 262–264.
- (22) Chen, L. X. *J. Electron Spectrosc. Relat. Phenom.* **2001**, *119*, 161–174.
- (23) Jennings, G.; Jager, W. J. H.; Chen, L. X. *Rev. Sci. Instrum.* **2002**, *73*, 362–368.
- (24) Shaw, G. B.; Grant, C. D.; Shirota, H.; Castner, E. W., Jr.; Meyer, G. J.; Chen, L. X. *J. Am. Chem. Soc.* **2007**, *129*, 2147–2160.
- (25) Chen, L. X.; Zhang, X.; Lockard, J. V.; Stickrath, A. B.; Attenkofer, K.; Jennings, G.; Liu, D. J. *Acta. Crystallogr. A* **2010**, *66*, 240–251.
- (26) Westre, T. E.; Kennepohl, P.; DeWitt, J. G.; Hedman, B.; Hodgson, K. O.; Solomon, E. I. *J. Am. Chem. Soc.* **1997**, *119*, 6297–6314.
- (27) Della Longa, S.; Girasole, M.; Congiu Castellano, A.; Bianconi, A.; Kovtun, A. P.; Soldatov, A. V. *Eur. Biophys. J.* **1998**, *27*, 541–548.
- (28) Chen, L. X. *Annu. Rev. Phys. Chem.* **2005**, *56*, 221–254.
- (29) Chen, L. X. *Angew. Chem., Int. Ed. Engl.* **2004**, *43*, 2886–2905.
- (30) Schotte, F.; Lim, M.; Jackson, T. A.; Smirnov, A. V.; Soman, J.; Olson, J. S.; Phillips, G. N.; Wulff, M.; Anfinrud, P. A. *Science* **2003**, *300*, 1944–1947.
- (31) Franzen, S.; Kiger, L.; Poyart, C.; Martin, J.-L. *Biophys. J.* **2001**, *80*, 2372–2385.
- (32) Kitagawa, T.; Haruta, N.; Mizutani, Y. *Biopolymers* **2002**, *67*, 207–213.
- (33) Dao, L. V.; Lowe, R. M.; Rowlands, W. J.; Lincoln, C. N.; Hannaford, P. In *Femtochemistry And Femtobiology*; Douhal, A. a. S. J., Ed.; World Scientific Publishing Co., Pte. Ltd.: River Edge, NJ: 2002; pp 815–819.
- (34) Belogortseva, N.; Rubio, M.; Terrell, W.; Mikšovská, J. *J. Inorg. Biochem.* **2007**, *101*, 977–986.
- (35) Ressler, T. *J. Synchrotron Radiat.* **1998**, *5*, 118–122.
- (36) Ankudinov, A. L.; Bouldin, C. E.; Rehr, J. J.; Sims, J.; Hung, H. *Phys. Rev. B* **2002**, *65*, 104107.
- (37) Ankudinov, A. L.; Ravel, B.; Rehr, J. J.; Conradson, S. D. *Phys. Rev. B* **1998**, *58*, 7565–7576.
- (38) Sayers, D. E.; Stern, E. A.; Lytle, F. W. *Phys. Rev. Lett.* **1971**, *27*, 1204–1207.
- (39) Lytle, F. W.; Sayers, D. E.; Stern, E. A. *Phys. Rev. B* **1975**, *11*, 4825–4835.
- (40) Stern, E. A.; Sayers, D. E.; Lytle, F. W. *Phys. Rev. B* **1975**, *11*, 4836–4846.
- (41) Hasnain, S. S.; Hodgson, K. O. *J. Synchrotron Radiat.* **1999**, *6*, 852–864.
- (42) Hasnain, S. S.; Strange, R. W. *J. Synchrotron Radiat.* **2003**, *10*, 9–15.